

Effective Shielding of $\lesssim 10$ GeV Cosmic Rays from Dense Molecular Clumps

Rui-zhi Yang^{1,2,3}, Guang-Xing Li⁴, Emma de Oña Wilhelmi⁵, Yu-Dong Cui⁶, Bing Liu^{1,2,3}, Felix Aharonian^{7,8,9}

¹Deep Space Exploration Laboratory/School of Physical Sciences, University of Science and Technology of China, Hefei 230026, China

²CAS Key Laboratory for Research in Galaxies and Cosmology, Department of Astronomy, University of Science and Technology of China, Hefei, Anhui 230026, China

³School of Astronomy and Space Science, University of Science and Technology of China, Hefei, Anhui 230026, China

⁴South-Western Institute for Astronomy Research (SWIFAR), Yunnan University (YNU), Kunming 650500, People's Republic of China

⁵Deutsches Elektronen Synchrotron DESY, 15738 Zeuthen, Germany

⁶School of Physics and Astronomy, Sun Yat-Sen University, Guangzhou, 510275, China

⁷Dublin Institute for Advanced Studies, 31 Fitzwilliam Place, Dublin 2, Ireland

⁸Max-Planck-Institut für Kernphysik, P.O. Box 103980, D 69029 Heidelberg, Germany

⁹Gran Sasso Science Institute, 7 viale Francesco Crispi, 67100 L'Aquila, Italy

The density of cosmic rays inside molecular clouds determines the ionization rate in the dense cores where stars form. It is also one of the drivers of astrochemistry leading to the creation of complex molecules. Through Fermi Large Area Telescope observations of nearby giant molecular clouds, we observed deficits (holes) in the gamma-ray residual map when modelling with the expected gamma-ray diffuse emission from uniform cosmic rays interacting with the molecular content. We propose that the deficit is due to the lack of penetration of the low-energy (sub-GeV to GeV) cosmic rays into denser regions or clumps. This differs from the prevailing view of fast cosmic ray transport in giant molecular clouds where the magnetic turbulence is suppressed by neutral-ion damping, as our results require a slow diffusion inside dense molecular clumps. Through modelling we find that while the shielding is negligible on the cloud scale, it becomes important in the denser, parsec-sized regions where the gravitational collapse is already at play, changing the initial condition of star formation and astrochemistry.

Cosmic rays (CRs) are one of the most important ingredients in the interstellar medium (ISM), with an energy density similar to that of the magnetic field and the thermal energy of the gas. The interplay between star formation and CRs is one of the most important physical processes in astrophysics. The star formation process can be regarded as the ultimate energy source of CRs, as the stars either accelerate CRs through the stellar winds¹ or via supernova remnants and compact objects at later stages of their evolution, whereas the CRs generated by star formation can change the initial condition of star formation as well as the astrochemistry processes therein.

Star formation occurs in giant molecular clouds (GMCs). These massive cloud-like entities are made of cold, molecular gas. CRs also play an essential role in star formation. CRs govern the heating and ionization processes in the star-forming regions², affect the dynamical evolution of gas, and initiate several crucial chemical reactions in the dense cores of molecular clouds³. The CR density may even affect the outcome of the star formation measured in terms of the initial mass function³. In the Milky Way, CRs permeating these dense clouds, lead to an excess of gamma-rays, which emerge from the interaction between the CRs and the matter. As a result, GMCs are also regarded as CR barometers⁴.

The transport of CRs within GMCs is a difficult problem, since GMCs are also complex, evolving objects which exhibit density fluctuations on all observable scales⁵. In the Milky Way, these clouds have surface densities of a few tens of solar mass per parsec²^{6,7}. Inside a cloud, denser, pc-sized regions called clumps have been observed⁸. Several studies suggest that although GMCs are gravitationally unbound⁹, the dense clumps are pc-sized gravitationally-bound objects whose collapse leads to clustered star formation^{10,11}. The significant density variations can lead to a non-homogeneous distribution of CRs. Moreover, the presence of magnetic fields in clouds is one further complication. Although studies have suggested that the magnetic field strength can be damped in clouds¹², observations have pointed to moderate magnetic fields ($\approx 10\mu G$) whose strength increases with the gas density¹³. The high density and strong magnetic field should form a barrier for CR propagation. This shielding effect might be augmented by the fact that the clumps have centrally condensed density profiles¹⁴⁻¹⁶. Using Fermi Large Area Telescope (Fermi-LAT) gamma-ray data, we study the shielding of CRs in dense clumps and find evidence where slow propagation is required to explain the gamma-ray deficiency. This slow propagation leads to non-homogeneous CR distributions in clouds.

1 CR deficit in dense molecular clumps

We chose Taurus and Perseus clouds to search for the effect of possible shielding of CRs in dense clumps. Located in different layers of the Taurus-Auriga-Perseus complex, the largest local associations of dark nebula¹⁷, Taurus and Perseus are among the nearest GMCs to the Earth, whose distances are estimated as 100 – 200 pc and ~ 300 pc, respectively¹⁸. In the vicinity of these clouds, both low mass and high mass star formations have been observed¹⁹. They are amongst the GMCs with the largest M/d^2 values, where M is the mass and d is the distance to the solar system. This parameter is crucial for the predicted gamma-ray flux of the GMCs²⁰, which is proportional to M/d^2 . High gamma-ray detection significance allows more accurate spatial and spectral analysis,

which is required in this work.

We use Planck dust opacity maps to trace the gas distributions. A detailed description can be found in the Methods. The derived gas column density map is shown in Fig. 1, in which we identified six dense clumps with average cubic density higher than 5000 cm^{-3} . Of those clumps, five were selected for our investigation (dubbed C1-5), whereas the sixth one is disregarded, as it coincides with the star formation region IC 348. The gamma-ray emission in the direction of IC 348 shows different properties and shall be considered independently (Methods).

We analysed about 12 years of Fermi-LAT gamma-ray data (above 100 MeV) towards the Taurus-Perseus region (see Methods for details on the analysis). The observed gamma-ray emission in the field of view results from the CR sea interacting with the molecular content (diffuse background) and individual sources. The former includes the information we want to derive, where we use a template obtained from the Planck dust opacity²¹. The latter is modelled using the fourth source catalog of Fermi-LAT (4FGL) catalogue²². A detailed description of how the diffuse background model was obtained can be found in the Methods. The diffuse gamma-ray model should be much more complex than the gas distributions traced by the Planck dust opacity, but in the high latitude region as the one in here, and given the proximity of the GMCs, the total gas in the line of sight is dominated by the GMCs. In such a scenario, the assumption that the gas distribution has a similar spatial distribution to the gamma-ray emission is a good approximation. The usage of dust opacity as the background template also allows us to separate the dust emission from a different line of sight and derive the CR distribution in different regions. To validate our results, we compared our results with the ones obtained using the galactic diffusion emission model provided by the Fermi collaboration and used in the standard analysis. The consistent existence of the negative residuals showed in Supplementary Fig. 1 and 2 demonstrates that the adopted model based on the dust distribution is correct for this region.

We separated the Planck dust opacity template into diffuse envelope and dense cores, of which the gas column density is below and above $1.8 \times 10^{22} \text{ cm}^{-2}$, respectively. We found such separation can improve the likelihood fitting significantly when comparing with the fitting without such separation, which implies that the gamma-ray emission from the diffuse envelope and dense cores may have different spectra. This separation also allows us to derive the diffuse spectra of gamma-rays in regions of lower density (envelope) and dense ones (cores). Then we normalized the gamma-ray emission to the emissivities per H atom, which should be proportional to the CR density. The results are shown in the left panel of Fig. 2. We found that the gamma-ray emissivities derived in the diffuse envelope are consistent with the predicted gamma-ray emissivities, assuming the CR spectra are the same as the local interstellar spectra (LIS). For dense cores, however, the measured gamma-ray emissivities exhibit significant localized deficits at lower energies ($E < 2 \text{ GeV}$).

One possible explanation of such a deficit of low-energy gamma-rays is that the gas column density of the dense core is overestimated, which lowers the gamma-ray flux consequentially. This would imply a significantly lower gas-to-dust ratio in dense cores. Indeed, such a variation of the gas-to-dust ratio has already been observed inside the dense core ρ Oph A²³. However, the very

low gas-to-dust ratio is only observed in the very central region of the core (< 0.05 pc), which is far below the resolution of gamma-ray instruments. On the scale of the core of several parsecs, the average gas-to-dust ratio estimated in ref ²³ is consistent with the average value in our Galaxy. Stronger evidence against the interpretation is that in almost all our cases, the deficit appears to be stronger for CRs of lower energies, and an overestimation of the gas column density would affect the normalization of the spectrum but not the shape. The different spectral shapes (as shown in Fig. 2) point rather to different CR spectra at different regions.

We further derived the CR spectra from the observed gamma-ray emissivities. Here, we assumed a smoothed broken power-law spectrum for parent CR protons, that is:

$$N_p(E) = A_0 E^{-a_1} (1 + (E/E_c)^{a_2 - a_1})^{-1}, \quad (1)$$

where N_p is the proton density, E is the kinetic energy of CR protons, A_0 is the normalization factor, a_1 and a_2 are the spectral indices below and above the cutoff energy E_c , respectively. We note that the low-energy data points are not very constraining if a_1 is free, thus, we fixed a_1 to be 1 in the fitting. The derived a_2 and E_c for diffuse envelope and dense cores are $a_2 = 3.01 \pm 0.06, E_c = 2.71 \pm 0.65$ and $a_2 = 2.87 \pm 0.10, E_c = 3.66 \pm 1.20$, respectively. The full covariance matrix is used when deriving the CR proton flux, which is shown in the right panel of Fig. 2. The indications of the CR spectra are consistent with those of the gamma-ray emissivities, that is, the CR in the diffuse envelope has nearly identical spectrum as the LIS, while in the dense cores, the CR density is significantly lower below a few GeV, and became consistent with LIS at higher energies.

The CR deficit at low energies has three possible origins. Firstly, similar to the ‘solar modulation’ effects in the solar system, this may be due to the young stars formed already inside these dense cores producing strong stellar winds, which prevent the CRs in the ISM to enter the dense cores. Such an effect has also recently been adopted to explain the low CR density in the central molecular zone and other regions^{20,24}. The effectiveness of this mechanism depends on the overall strength of the stellar winds driven by young stars. The star formation in Perseus and Taurus differs vastly from one region to other²⁵, which would result in major differences in the CR deficit from cloud to cloud. With the current data, we did not find significant difference in the gamma-ray spectra for different clumps (Methods), although given the current statistics, we cannot rule out such a scenario yet. Additionally, protostellar outflows are collimated objects, with opening angles ranging from a few degrees for young objects to tens of degrees for evolved objects²⁶. Although these regions might contain a few of these outflows, the outflow cavities are not volume-filling, and their role in CR shielding should be limited. In view of the above arguments, we would not discuss such a scenario in detail.

The magnetic mirroring effects can also prevent CRs entering the dense clumps. As estimated in ref ²⁷, the CR flux can be decreased by about 50% in the clumps compared with the cores. However, such an effect is also energy independent and thus contradicts to the different spectral shapes observed by gamma-rays (also see the Methods for details). Thus, the magnetic mirroring cannot account for the entire CR deficit. We note that the effect of the magnetic mirroring is estimated based on the method in ²⁷, in which the time evolution of magnetic fields is neglected. Detailed calculations based on more realistic assumptions is a subject of future studies.

2 Slow CR diffusion in clumps

A third explanation that seems to be favoured by our observations is a slower diffusive transport inside the dense cores, which has already been studied in ref ²⁸. Under this scenario, the CR deficit is caused by a combined effect of increased proton-proton absorption and slower diffusion caused by an increased magnetic field ^{29,30,30,31}. Since these factors are independent on star-forming process, it can explain why CR deficit occurs to all of our clumps. Additionally CRs of higher energies have larger gyroradii, and should diffuse faster ³², therefore the deficit would naturally be stronger for protons of lower energies.

To apply this hypothesis to our observations, we describe the CR transport adopting the equation in ref ²⁸, that is, CR transport is dominated by the diffusion equation with energy loss:

$$\frac{dN}{dt} = \frac{1}{R^2} \frac{\partial}{\partial R} (D(R, E) R^2 \frac{\partial N}{\partial R}) + \frac{\partial}{\partial E} (\dot{E} N), \quad (2)$$

where N is the space- and energy-dependent particle distribution function of CRs, R is the distance to the center of the clump, D is the diffusion coefficient, and \dot{E} is the energy loss rate of CR protons including both ionization loss and nuclear interaction loss. We assume a spherical clump with density profile of $n(R) = \frac{8000 \text{ cm}^{-3}}{0.04 + (R/1 \text{ pc})^2}$, and impose the boundary condition $N(R_{\text{mc}}) = N_{\text{lis}}$, where R_{mc} presents the clump boundary, and F_{lis} is the LIS CR density and a reflective (symmetric) boundary condition at $R = 0$. The normalizations are adjusted such that a total of $1800 M_{\odot}$ is contained in a region of $\sim 1 \text{ pc}$, which is consistent with the clump parameters in Table 1. Applying the above conditions, and for a stationary solution ($\frac{dN}{dt} = 0$), we can constrain the diffusion coefficient by fitting the derived CR spectrum. In this work we used a generic form $D(E) = D_0 (\frac{E}{1 \text{ GeV}})^{\Gamma}$, where D_0 is the diffusion coefficient 1 GeV at 1 GeV and Γ is the index reflecting the energy dependence.. Since Γ is highly unknown, we varied it within the reasonable limits to constrain the value of D_0 . Namely, changing Γ within the physically realistic limits from 0 (energy-independent diffusion) to 1 (Bohm-type diffusion) we found that D_0 cannot be outside the interval $2 \times 10^{26} - 6 \times 10^{26} \text{ cm}^2/\text{s}$. Thus, we arrive a robust conclusion that the diffusion coefficient around 1 GeV should be smaller than the one in the ISM by two orders of magnitude. Three schematic fittings with different Γ are shown in the right panel of Fig. 2.

We conclude that our observations required a slower diffusion characterized by a smaller diffusion coefficient. This stands in contrast to what was expected in these regions. According to the prevailing view¹², the magnetic turbulence should be damped out in the dense neutral gas environment, such that the propagation inside these dense cores should be dominated by free streaming or advection. The faster transport leads to an effective diffusion coefficient that is larger than those in the ISM ^{12,33}, which contracts the observational results. However, recent studies reveal that the magnetic field strength increases with the gas density ³⁴, with, for example, $B \propto \rho^{1/2}$. This can be explained if the energy density of the magnetic field is a fixed fraction (f_B) of that of the kinetic motion, which is further tied to the potential energy if the system is virialized ²⁹⁻³¹. The increased magnetic field in denser regions leads to slower CR diffusion. This scenario can potentially explain the decrease of CRs in dense regions. Another possibility is the magnetic turbulence

induced by CR streaming instability, which will also result in a slower diffusion inside dense clouds³⁵. Possible tests to distinguish these two scenarios are the GeV gamma-ray observations on clouds near CR accelerators, such as the molecular clouds interacting with supernova remnants³⁶, where the CR density are expected to be higher than the nearby GMCs. If the magnetic turbulence is increased mainly due to CR streaming instability, high CR density would imply more severe shielding. However, such supernova remnant-molecular cloud systems are all quite distant and the angular resolutions of current GeV gamma-ray instruments make such study rather difficult.

The Galactic molecular ISM contains density fluctuations over all scales. Having established the mechanism of magnetic shielding, we establish a picture of the effectiveness of magnetic shielding under different conditions. We assume that the clumps are virialised and that the magnetic energy density is comparable to the kinetic energy density. The condition for effective shielding can be derived through $\tau_{\text{diffusion}} = \tau_{\text{pp}}$, as other effects such as advective transport can be neglected²⁸. Here $\tau_{\text{diffusion}}$ and τ_{pp} are the diffusion and cooling time scale, respectively. $\tau_{\text{diffusion}} \approx r_{\text{clump}}^2/D$, where D is the diffusion coefficient and r_{clump} is the physical size of the clump. Since the inelastic scattering cross section of proton-proton collision is only weakly energy-dependent, $\tau_{\text{pp}} \propto n_{\text{clump}}^{-1}$, where n_{clump} is the average gas density in the clump. We assume $D \propto B^{-\gamma} E^\gamma$, where $\gamma < 1$ is needed to account for a possible suppression of the diffusion coefficient inside the turbulent cloud (in the following we adopt $\gamma = 1/2$)^{32,37,38}.

Using Zeeman measurement, observations³⁹ found out a positive correlation between the gas density and magnetic field strength, a trend that was later refrained by further observations³⁴. This positive correlation can be understood in framework where the magnetic energy density follows the kinetic energy density³¹ $B^2/8\pi \approx 1/2 n_{\text{clump}} \sigma_v^2$, where σ_v^2 is the velocity dispersion in the clump. If clumps are self-gravitating and virialized, for example, $\sigma_v = (Gm_{\text{clump}}/r_{\text{clump}})^{1/2}$, this scaling relation allows us to estimate the magnetic field strength for clumps of different masses and radii. Thus from $\tau_{\text{diffusion}} = \tau_{\text{pp}}$ we derive a relation between shielding energy E_s and the clump parameters, that is, $E_s \propto \frac{m_{\text{clump}}^3}{r_{\text{clump}}^4}$ (where m_{clump} is the clump mass), below which the shielding effect is substantial. The details can be found in the section ‘A general model for CR diffusion’ in the Methods. Shielding becomes effective above the threshold of clump mass

$$\left(\frac{m_{\text{clump}}}{1800 M_\odot}\right) = \left(\frac{r_{\text{clump}}}{1 \text{ pc}}\right)^{4/3} \left(\frac{E_s}{1 \text{ GeV}}\right)^{1/3}. \quad (3)$$

In Fig. 3, we plot the thresholds for effective shielding on the mass-size plane, where locations of molecular clouds⁶ and clumps⁴⁰ are also overlaid. The shielding effect is not important on the cloud scales, but becomes notable for the clumps with significantly increased densities.

3 Conclusions

The CRs inside GMCs determine the ionization rate and temperature of the molecular gas and affect the star formation process. The CR density is a crucial parameter in ISM modeling, yet

its value is poorly constrained due to our limited understanding of CR propagation. In this Article, for the first time, we find evidence that GeV and sub-GeV CRs, a dominant source of molecular ionization and a major driver of astrochemistry, do not penetrate deep into the dense core of GMCs, leading to localized negative regions (holes) in the gamma-ray residual maps. The effect is more pronounced at lower CR energies. A direct implication of our results here is the lower ionization rate in these dense clumps. Indeed, the anti-correlation between ionization rates and gas column densities has already been revealed from previous astrochemistry observations⁴¹, although not for the exact clumps we investigated in this work.

We propose that the CR deficit is caused by slower diffusion in the cloud. This slower diffusion of CRs contradicts the prevailing view where magnetic turbulence is suppressed by neutral-ion damping¹², which enables CRs to penetrate freely into the dense cores. On the contrary, the diffusion should be slower in the dense, star-cluster-forming clumps, where the magnetic field is stronger because the energy density of magnetic field follows the energy density of, for example, turbulent motions³¹. This scenario also explains the energy-dependent CR deficit as indicated by our observations.

Another possibility is that there is a small region separating the dense clumps from the more diffuse cloud, possibly due to CR self-generated waves^{33,35,42}, in which the CR diffusion is suppressed. In this case the CR propagation inside clumps can still be dominated by free streaming. The CRs deficit is caused by a barrier at the clump boundary rather than the slow diffusion inside dense clump.

Molecular clouds are objects with significant density fluctuations caused by turbulence and gravity, forming various barriers for CR transport. To describe this process, we propose a self-consistent model to describe the transport of CRs in different regions and find effective shielding occurs at the upper left part of the mass-size plane, above the threshold estimated in Eq.3. The shielding effect is important in dense, gravitationally bound regions which are believed to be star-cluster progenitors. In cloud evolution, gravitational collapse creates high-density regions, where the CR density is reduced and the initial condition of star formation is modified.

Method

Gas distributions and Clump Properties The column density of molecular hydrogen is often estimated using the integrated brightness temperature of the CO emission W_{CO} multiplied by the H_2/CO conversion factor X_{CO} . Then, the total gas column density N_{H} can be approximated as $N_{\text{HI}} + 2X_{\text{CO}}W_{\text{CO}}$, where N_{HI} is the column density of neutral hydrogen (HI). However, such estimation could miss the 'dark gas' that cannot be traced by CO emission. Thus, for a more robust and reliable result, we use the Planck dust opacity map²¹ to derive the gas distribution, given that the dust opacity is free of the 'dark gas' problem⁴³. According to Eq. (4) of ref.⁴⁴, the gas column density can be calculated by applying its relation to the dust opacity τ_{M} ,

$$N_{\text{H}} = \tau_{\text{M}}(\lambda) \left[\left(\frac{\tau_{\text{D}}(\lambda)}{N_{\text{H}}} \right)^{\text{ref}} \right]^{-1}. \quad (4)$$

Here τ_{M} is a function of the wavelength λ . And for the reference dust emissivity measured in low- N_{H} regions, $(\tau_{\text{D}}/N_{\text{H}})^{\text{ref}}$, we adopted the parameters at 353 GHz from Table 3 of ref.²¹ for the calculation. Note that the dust opacity map contains no velocity information, thus it is impossible to determine the gas content at different distances. However, the Taurus and Perseus region is located at relative high latitude ($b \approx -20^\circ$), and it is natural to assume that the total gas in the line of sight is at a similar location within the Galaxy. The map of gas column density is shown in Fig. 1.

The total mass of the cloud in each pixel can be obtained from the expression

$$M_{\text{H}} = m_{\text{H}} N_{\text{H}} A_{\text{ang}} d^2, \quad (5)$$

where m_{H} is the mass of the hydrogen atom, N_{H} is the total column density of the hydrogen atom in each pixel, A_{ang} is the angular area, and d is the distance. We chose five clumps in the Taurus and Perseus region, whose mass and locations are shown in the Table 1 and Fig. 1, respectively.

Fermi-LAT data We selected the Fermi Pass 8 data toward the Taurus and Perseus GMCs from 4 August 2008 (MET 239557417) until 17 January 2020 (MET 600946581) for the analysis, and chose a $20^\circ \times 20^\circ$ square region centered at the position of (R.A. = 61.66° , Dec. = 32.50°) as the region of interest (ROI). We chose the SOURCE class events with zenith angles less than 90° to reduce the contamination from the Earth's albedo. In addition, we applied the filter expression '(DATA_QUAL > 0)&&(LAT_CONFIG == 1)' to select the data of good time intervals that are not affected by spacecraft events. The Fermitools from the Conda distribution available at <https://github.com/fermi-lat/Fermitools-conda/>, and the P8R3 version of the instrument response functions *P8R3_SOURCE_V3* are used in the data analysis.

In the background model, we included the sources in the Fermi eight-year catalog²² within the ROI enlarged by 7° . We left the normalizations and spectral indices free for all sources within our ROI. For the diffuse background components, we first applied the standard Galactic diffuse model using the updated template *gll_iem_v07.fits* and isotropic emission model *iso_P8R3_SOURCE_V3_v1.txt*

(available at <https://fermi.gsfc.nasa.gov/ssc/data/access/lat/BackgroundModels.html>) setting their normalization parameters and the index of the Galactic diffuse emission free (such background models are dubbed as Fermi background below). Since we are investigating the diffuse emission itself, we also build a background model based on the gas distribution to investigate the spectral characteristics of the diffuse emission in regions of different density. The later is built from the gas distribution derived from the Planck dust opacity map ²¹ (Planck background model). The galactic diffuse emission basically includes the contributions from the inverse Compton (IC) scattering off soft high energy electrons, as well as π^0 decay and bremsstrahlung that take place in the H I and H₂ regions. To estimate the background, we calculated the contributions from IC using GALPROP (<http://galprop.stanford.edu/webrun/>) ⁴⁵, which uses information regarding CR electrons and the interstellar radiation field. Isotropic templates related to the CR contamination and extragalactic gamma-ray background were also included in the analysis ⁴⁶. And finally we included a background template generated from dust opacity maps derived by the Planck collaboration ²¹, where we assumed that gamma-rays trace the spatial distribution of the gas. We chose the size of this background template 10 degrees larger than our ROI, to account for the limited angular resolution in the Fermi-LAT data. We named such background model as 'dust background'.

Spatial structure To take advantage of the better angular resolution, we used the events above 1 GeV to study the spatial distribution of the gamma-ray emission. We note that there are three point-sources (4FGL J0341.9+3153, 4FGL J0344.2+3203, 4FGL J0346.2+3235) in the vicinity of the star cluster IC348. To study the excess gamma-ray emission around IC348, we excluded these three 4FGL sources from our background model. We first used the Fermi background model. After the likelihood fitting, we subtracted the best-fit diffuse model and all the remaining sources in the ROI, the resulting residual maps are shown in Supplementary Fig.1. We find strong residuals towards the direction of IC 348 region (marked as cyan circle and square), while there are 'negative' residuals in the vicinity of other dense cores.

To study the morphology of the gamma-ray emission located at the position of IC 348, we added a uniform disk on top of the model used in the likelihood analysis. We then varied the position and size of the disk to find the best-fit parameters. We compared the overall maximum likelihood of the model with (L) (alternative hypothesis) and without (L_0) (null hypothesis) the uniform disk, and define the test statistics (TS) of the disk model $-2(\ln L_0 - \ln L)$ following ref ⁴⁷. The best-fit result is a disk centered at (R.A. = $55.98^\circ \pm 0.10^\circ$, Dec. = $32.01^\circ \pm 0.10^\circ$) with $r_{\text{disk}} = 0.8^\circ \pm 0.10^\circ$, with a TS value of 140, corresponding to a significance of more than 12σ . We also tested whether this extended emission is composed of several independent point sources. To do this, we recovered the 3 point sources in the likelihood model. Although with more free parameters, the-log(likelihood) function value is larger than that in the 2D disk template case. Thus in the following analysis, we used the best-fit disk as the spatial template.

To check whether the negative residuals in the dense cores are from the systematic uncertainty related with the Fermi standard background models, we fixed the normalization of the Galactic diffuse template to be 6% higher or lower than the best-fit value by hand in the likelihood fitting

following the same method used in ref ⁴⁸. The derived residual maps are also shown in Supplementary Fig.1. We found that, as expected, the fitting is worse than the case when the normalization of Galactic background template are left free, but the 'negative' residual are still significant.

We also used the dust background model to repeat the process. The residual map above 1 GeV is shown in the right panel of Supplementary Fig.2. In this case, there are also significant extended excesses observed towards HH211/IC 348. The best-fit result is a disk centered at (R.A. = $55.48^\circ \pm 0.10^\circ$, Dec. = $31.89^\circ \pm 0.10^\circ$) with $r_{\text{disk}} = 0.7^\circ \pm 0.1^\circ$, with a TS value of 70, corresponding to a significance of more than 8σ .

As shown in Supplementary Fig.1 and Supplementary Fig.2, we note that these negative residuals spatially coincide with the densest clumps (marked as C1 to C5). We note that in fact the star cluster IC 348 also coincides with a dense molecular clump. To test the possible inhomogeneous distribution of CRs inside MCs, we divided the Planck background into dense core and diffuse envelop, with the gas column above and below $1.8 \times 10^{22} \text{ cm}^{-2}$, respectively. The corresponding gas templates are shown in Supplementary Fig.3. In the likelihood fitting, we have 5 diffuse components, which are IC and isotropic background, the dense core and diffuse envelop of gas distributions, and the 0.8° disk template to model the excess in IC 348 regions. We name such a spatial model as dense + diffuse below. Using the 5 diffuse components described above, together with all the 4FGL sources excluding 4FGL J0341.9+3153, 4FGL J0344.2+3203, and 4FGL J0346.2+3235, the negative residuals are significantly reduced, as shown in the right panel of Supplementary Fig.2. The improvement of the likelihood fitting are also shown in the $-\log(\text{likelihood})$ value as shown in Supplementary Table 1. The TS value ($-2(\ln L_0 - \ln L)$) of the dense + diffuse model are about 700, considering the 2 additional free parameters in this model compared with the dust model, the significance is about 26σ .

To check whether the negative residuals are due to limited angular resolution, we repeated above analysis procedure using Fermi-LAT data of PSF 3 event class, which has better angular resolution than the SOURCE event class. The derived residual with dust model is shown in the middle panel of Supplementary Fig.2, which reveals a similar negative residual as in the SOURCE event class. The dense + diffuse model also significantly improve the fitting (see Supplementary Table 1), the TS are about 130. To further test the possible influence by other diffuse components, we also increase and decrease the normalization of IC and isotropic components by hand in the likelihood fitting, and the results are also shown in Supplementary Table 1. The TS of the dense + diffuse models are also about 700 in these two cases.

The derived photon index for the disk templates of IC348 above 1 GeV is 2.2 ± 0.1 , and the total gamma-ray flux can be estimated as $(1.2 \pm 0.2) \times 10^{-9} \text{ ph.cm}^{-2}.\text{s}^{-1}$ above 1 GeV, which reads $(6.0 \pm 1.2) \times 10^{34} \text{ erg.s}^{-1}$ above 1 GeV, if we assume a distance of 310 pc and a single power law spectrum.

Spectral analyses To further investigate the spectral properties of the GeV emission and the underlying particle spectra, we used the spatial templates mentioned above, and divided the energy range from 0.1 GeV to 100 GeV into 10 logarithmically spaced energy bins and derived the spectral

energy distribution (SED) via the maximum likelihood analysis in each energy bin. The significance of the signal detection for each energy bin exceeds 2σ . Besides the 68% statistical errors for the energy flux densities, we also varied the normalization of isotropic and IC templates by 6% artificially to account for the systematic errors associated with the diffuse backgrounds⁴⁸. The SEDs for the dense core, diffuse envelope and the IC 348 region are shown in Supplementary Fig.4. Note that the gamma-ray fluxes are normalized to emissivity per H atom, which is proportional to the parent CR density.

To further test the possible statistics in the spectral analysis, we used slightly different spatial templates for the dense clumps. Instead of $1.8 \times 10^{22} \text{ cm}^{-2}$, we used the column density $1.3 \times 10^{22} \text{ cm}^{-2}$ and $2.3 \times 10^{22} \text{ cm}^{-2}$ above and below which we divided the dust template to dense core and diffuse envelope. As expected, with a lower column density cut the size of the dense core should be larger and the average density is lower. The derived SEDs for both cases are shown in Supplementary Fig.5. We found for both cases the gamma-ray emissivities are suppressed compared to LIS in low energy range, and the suppression is more significant when the column density cut is $2.3 \times 10^{22} \text{ cm}^{-2}$, this is also expected due to a higher density and thus stronger CR shielding. Finally, we also derived the SEDs using the PSF3 events with model of Fermi-LAT to take advantage of the best angular resolution. The results are also shown in Supplementary Fig.5, which is in good agreement with the results by using SOURCE data.

We also derived the gamma-ray SEDs from the individual clumps to see whether there is any difference, the results are shown in Supplementary Fig.6. Due to the limited statistics, we cannot claim significant difference in the derived spectra in different clumps.

Deriving the CR proton spectrum The CR spectra are derived assuming the CR spectrum have the function form of broken power-law, that is:

$$N_p(E) = A_0 E^{-a_1} (1 + (E/E_c)^{a_2 - a_1})^{-1}, \quad (6)$$

where E is the kinetic energy of CR protons, a_1 and a_2 are the spectrum indices below and above the cutoff energy E_c , respectively. We note that the low energy data points are not very constraining, thus we fix a_1 to be 1. We then fit the observed gamma-ray emissivities using the gamma-ray production cross section parametrised in ref⁴⁹. The derived a_2 and E_c for diffuse envelope and dense cores are $a_2 = 3.01 \pm 0.06$, $E_c = 2.71 \pm 0.65$ and $a_2 = 2.87 \pm 0.10$, $E_c = 3.66 \pm 1.20$, respectively. We then used the full covariance matrix in the fitting to derive the CR proton flux and 1σ error regions as shown in the shaded area in the right panel of Fig. 2. And from Fig. 2 we found the CR fluxes below several GeV are significant lower in the dense cores than those in the diffuse envelope and LIS.

To see the energy range over which the CRs are effectively shielded, we also plot the predicted gamma-ray emissivities assuming different sharp low energy break E_c in the LIS, i.e., we assume the CR spectra are identical to LIS above E_c and zero below. The results are shown in Supplementary Fig.7, in which we found at least to up to 5 GeV the shielding of CRs should be significant.

Magnetic mirroring In dense clumps, due to the compression of the magnetic field lines, both the magnetic mirroring and focusing can alter the CR density inside the clumps. We used the method in ref²⁷ to estimate such effects. The scaling factor of CR flux inside the clumps is estimated as $\eta(\chi) = (\chi - \sqrt{\chi^2 - 1})$, where χ is the enhancement factor of magnetic field inside the clump compared with those in ISM. We note that $\eta(\chi)$ saturated to 0.5 quickly when $\chi > 2$. In Supplementary Fig.8 we plot the predicted CR density considering the magnetic mirroring, from which we found that the magnetic mirroring alone can hardly account for the different spectral shapes in clumps and envelopes. We found that such an energy-independent feature can hardly explain the derived CR spectra in clumps and envelopes. A combination of underestimation of mass in clumps as well as the slow diffusion and magnetic mirroring can fit the observations. But the underestimation of mass from the dust emission reveals a higher gas-to-dust ratio in the clump, which is in contrary with the observations in ref²³. Another possibility is that the simple evaluation of magnetic mirroring cannot reflect the complexities inside clumps, in which the magnetic fields can be highly turbulent and time-dependent.

IC 348 We then return to the positive residual towards IC 348. The derived gamma-ray SED and derived CR spectrum are shown in Supplementary Fig.9. We found the extra gamma-ray emission towards IC 348 can be best modelled with a uniform disk with a radius of $0.8^\circ \pm 0.1^\circ$, and the spectrum is significantly harder than LIS. We also note that the gamma-ray spectrum reveals a 'pion-bump' feature below 1 GeV, thus, we fit this gamma-ray component, assuming they are from the interaction of CRs with the ambient gas. We found the parent proton spectrum described by a power law in kinetic energy is sufficient to provide a satisfactory fit. The derived parent proton spectrum is also shown in the right panel of Supplementary Fig.9, and the best-fit parent proton spectral index is 2.2 ± 0.1 . We found that this is very similar to the CR spectra derived in young massive clusters (YMC), such as Cygnus Cocoon⁵⁰, Westerlund 2⁵¹, and NGC 3603⁵². Compared with these YMCs, the most massive star in IC 348 is of the spectral type B5, implying IC 348 should be much less powerful. But IC 348 is also much nearer than those YMCs. Although IC 348 and NGC 1333 reside in similar environments, that is, the dense cores in Perseus GMC, their spectra are quite different. While in NGC 1333, like in other dense cores, the CR spectrum reveals a suppression in low energy, in IC 348, an extra hard CR component is observed. Ref⁵³ studied the star census in both IC 348 and NGC 1333 in detail, and found that the young stars in IC 348 are much more massive than those in NGC 1333. So a tentative explanation would be that a hard component of CRs is accelerated by the massive stars in IC 348, just as the CRs accelerated by YMCs.

A general model for CR diffusion We build a comprehensive picture of CR propagation, which is similar to the one presented in⁴. We assume that the clumps are virialized where the velocity dispersion $\sigma_v = (Gm_{\text{clump}}/r_{\text{clump}})^{1/2}$, We assume that the energy density of the magnetic field follows the energy density of kinetic motion $B^2/8\pi \approx 1/2 f_B \rho_{\text{clump}} \sigma_v^2$, where ρ_{clump} is the cubic gas density inside the clump. Assuming clump-scale mean diffusion coefficient of $D = 1.5 \times$

$10^{26} \text{ cm}^2 \text{ s}^{-1} (B/10\mu\text{G} \times f_B^{-1/2})^{-1/2} (E/(1\text{GeV}))^{1/2}$, we find

$$\begin{aligned} n_{\text{H}_2, \text{clump}} &= \rho_{\text{clump}}/m_{\text{H}_2}/1.37 = m_{\text{clump}}/(4/3\pi r_{\text{clump}}^3)/m_{\text{H}_2}/1.37 \\ &\approx 4000 \text{ cm}^{-3} \left(\frac{m_{\text{clump}}}{1000 m_{\odot}}\right) \left(\frac{r_{\text{clump}}}{1 \text{ pc}}\right)^{-3}, \end{aligned} \quad (7)$$

where the $n_{\text{H}_2, \text{clump}}$ is the cubic density of molecular hydrogen, m_{H_2} is the mass of a molecular hydrogen, and the factor 1.37 takes the contribution of heavy elements into account. Then the magnetic field strength can be estimated as

$$B = (8\pi f_B^{-1/2} \rho_{\text{clump}} \sigma_v^2)^{1/2} = 96\mu\text{G} f_B^{-1/2} \left(\frac{m_{\text{clump}}}{1000 m_{\odot}}\right) \left(\frac{r_{\text{clump}}}{1 \text{ pc}}\right)^{-2}. \quad (8)$$

The diffusion time is

$$\begin{aligned} \tau_{\text{diffusion}} &= \frac{r_{\text{clump}}^2}{2D} = \frac{r_{\text{clump}}^2}{1.5 \times 10^{26} \text{ cm}^2 \text{ s}^{-1} (B/10\mu\text{G})^{-1/2} (E/(1 \text{ GeV}))^{1/2}} \\ &= 3000 \text{ yr} \left(\frac{m_{\text{clump}}}{1000 M_{\odot}}\right)^{1/2} \left(\frac{r_{\text{clump}}}{1 \text{ pc}}\right) \left(\frac{E}{1 \text{ GeV}}\right)^{-1/2}. \end{aligned} \quad (9)$$

The time for pp collisional absorption is

$$\tau_{\text{pp}} \approx 2 \times 10^4 \text{ yr} \left(\frac{n}{3000 \text{ cm}^{-3}}\right)^{-1} \approx 7500 \text{ yr} \left(\frac{m_{\text{clump}}}{1000 M_{\odot}}\right)^{-1} \left(\frac{r_{\text{clump}}}{1 \text{ pc}}\right)^3. \quad (10)$$

and Eq.3 can be derived by equating $\tau_{\text{diffusion}}$ and τ_{pp} .

Data Availability

The Fermi-LAT data used in this work is provided online by the NASA-GSFC Fermi Science Support Center, and can be downloaded from the data serve <https://fermi.gsfc.nasa.gov/ssc/data/access/lat/>. The Planck dust opacity map is publicly available in Planck Legacy Archive (http://pla.esac.esa.int/pla/aio/product-action?MAP.MAP_ID=COM_CompMap_ThermalDust-commander_2048_R2.00.fits).

Code Availability

Fermi-LAT data used in our study were reduced and analysed using the standard FERMITOOLS V1.0.1 software package available from <https://github.com/fermi-lat/Fermitools-conda/wiki>.

Acknowledgments

Rui-zhi Yang is supported by the NSFC under grants 12041305, 11421303 and the national youth thousand talents program in China. Guang-Xing Li acknowledges supports from NSFC grant

clumps	center ¹	size ² ($r_{\text{maj}}, r_{\text{min}}$)	distance ³	mass ⁴ (M_{\odot})	average density ⁵ (Hcm^{-3})
C1	69.0, 25.8	1.52, 0.76	140 pc	2871	1.6×10^4
C2	67.8, 27.0	0.84, 0.41	150 pc	422	1.5×10^4
C3	67.87 24.4	1.83, 0.61	140 pc	1923	1.2×10^4
C4	64.1, 28.1	1.93, 1.0	140 pc	2363	0.6×10^4
C5	52.2, 31.1	1.40, 0.56	290 pc	2324	2.4×10^4

1. RA and Dec. 2. Ellipse a and b ($r_{\text{maj}}, r_{\text{min}}$), in parsec. 3. Distances taken from ⁵⁴. 4. The mass is calculated as $m = \int 1.37 N_{\text{H}} m_{\text{H}} ds$, where the factor 1.37 takes the contribution of heavy elements into account. 5. The density is computed using $n_{\text{H}} = m / (4/3 \pi r_{\text{mean}}^3) 1.37^{-1} m_{\text{H}}^{-1}$, where $r_{\text{mean}} = (r_{\text{maj}} r_{\text{min}})^{1/2}$.

Table 1: Parameters of the five clumps

1227030463, W820301904 and 12033005. Bing Liu acknowledges the support from the NSFC under grant 12103049. Yudong Cui is supported by Ministry of Education of China, and the China Manned Space Project (No. CMS-CSST- 2021-B09).

Author Contributions

Rui-zhi Yang, Guang-Xing Li and Bing Liu contributed to the paper in equivalent fractions. Rui-zhi Yang, Bing Liu and Emma de Ona Wilhelmi performed the data analysis, Guang-Xing Li, Rui-zhi Yang, Yu-dong Cui and Felix Aharonian were responsible for the interpretation part, all authors contributed to the manuscript writing.

Competing Interests

The authors declare no competing interests.

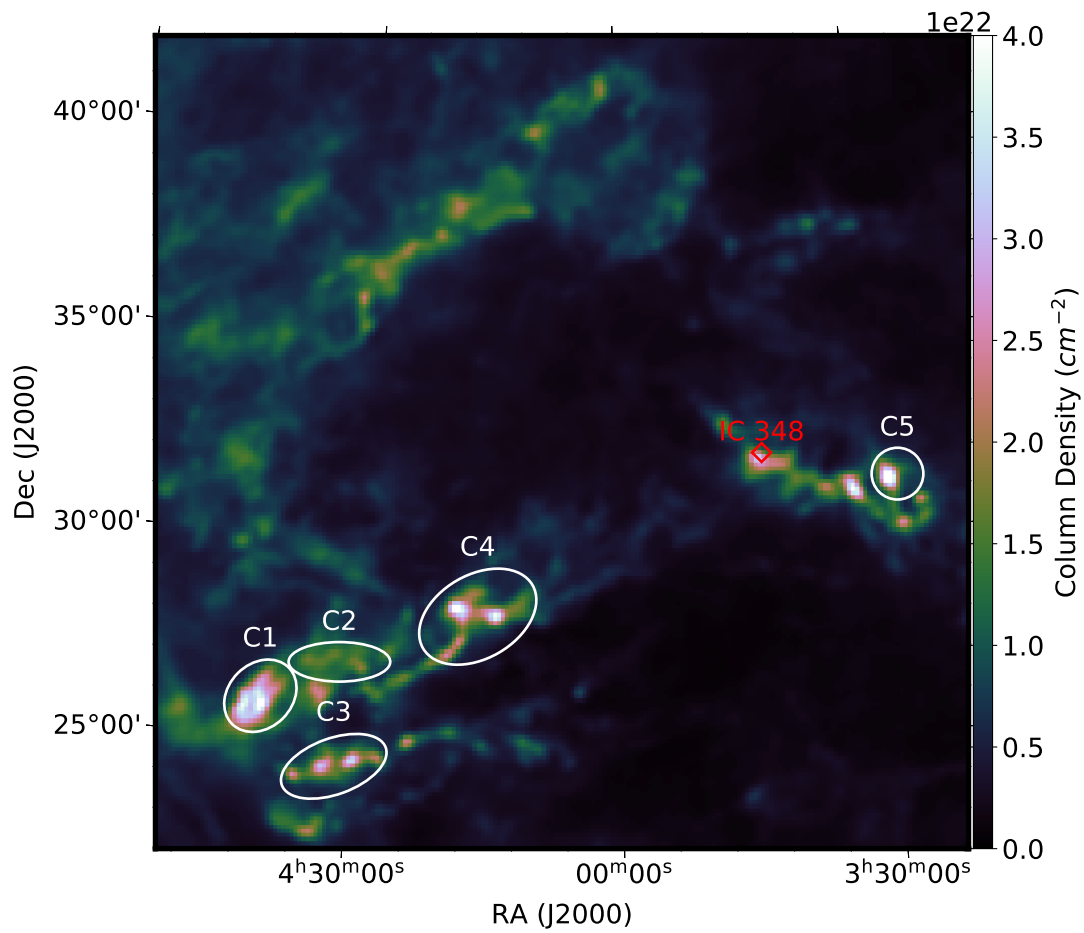


Figure 1: The total column density (in units of cm^{-2}) derived from the Planck dust opacity map and smoothed with a Gaussian kernel of 0.2° . The white ellipses show the position of dense molecular clumps, and the red diamond marks the position of the star cluster IC 348.

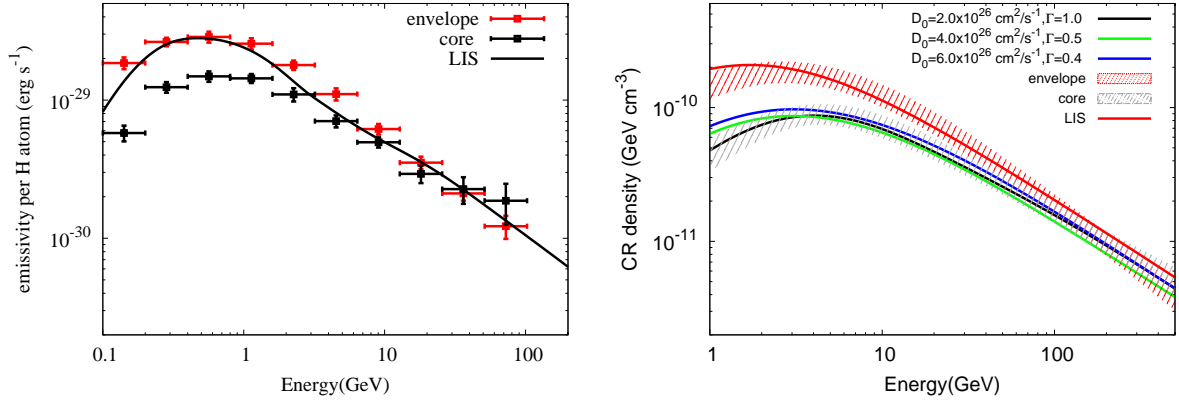


Figure 2: The gamma-ray spectra obtained from Fermi LAT observations and the derived CR energy density. left panel: The derived gamma-ray spectra of all the clumps normalized to gamma-ray emissivity per H atom both for dense and diffuse envelop. The x error bars represent the energy bin width, the y error bars are the $1 - \sigma$ statistical and systematic errors added in quadrature. The black curve represent the predicted gamma-ray emissivity assuming the CR spectra is the same as the LIS. right panel: derived CR energy density from the gamma-ray spectra. The red curve is the LIS. The shaded area represent the $1 - \sigma$ statistical and systematic errors for the derived CR density added in quadrature.

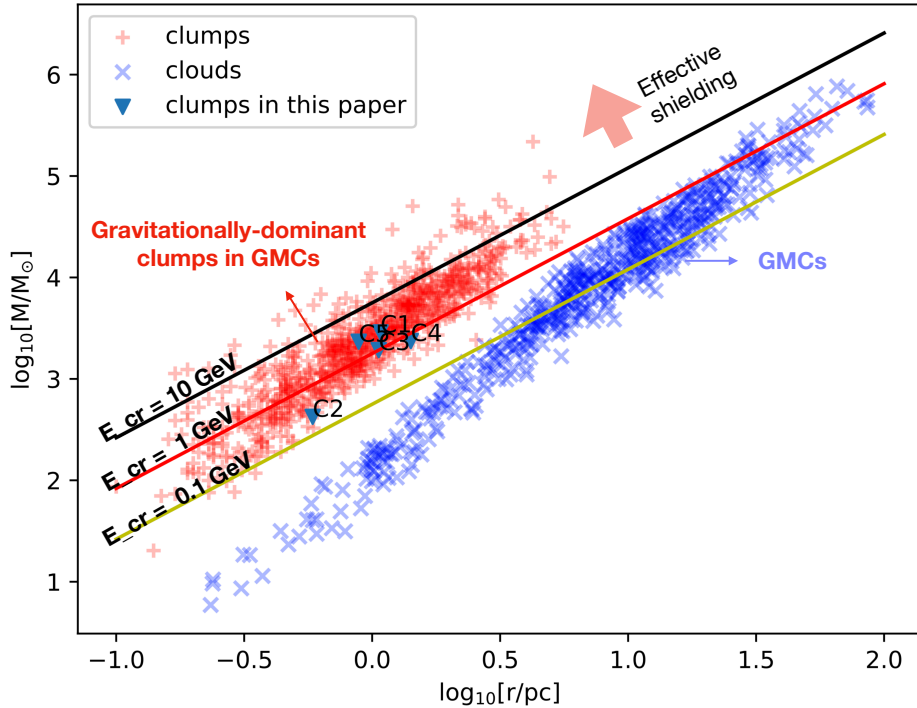


Figure 3: Shielding effect toward structures of different masses and sizes. The lines represent different thresholds above which shielding becomes important for CRs of different energies. Masses and sizes of molecular clouds⁶ and star cluster-forming clumps⁴⁰ are also overlaid. Shielding is not important on the cloud scale, but becomes significant in dense molecular clumps where the densities are much higher.

1. Aharonian, F., Yang, R. & de Oña Wilhelmi, E. Massive stars as major factories of Galactic cosmic rays. *Nature Astronomy* **3**, 561–567 (2019).
2. Dalgarno, A. Interstellar Chemistry Special Feature: The galactic cosmic ray ionization rate. *Proceedings of the National Academy of Science* **103**, 12269–12273 (2006).
3. Papadopoulos, P. P. A Cosmic-ray-dominated Interstellar Medium in Ultra Luminous Infrared Galaxies: New Initial Conditions for Star Formation. *Astrophys. J.* **720**, 226–232 (2010).
4. Aharonian, F. A. Gamma Rays From Molecular Clouds. *Space Sci. Rev.* **99**, 187–196 (2001).
5. Kainulainen, J., Beuther, H., Henning, T. & Plume, R. Probing the evolution of molecular cloud structure. From quiescence to birth. *Astron. Astrophys.* **508**, L35–L38 (2009).
6. Chen, B. Q. *et al.* A large catalogue of molecular clouds with accurate distances within 4 kpc of the Galactic disc. *Mon. Not. R. Astron. Soc.* **493**, 351–361 (2020).
7. Lada, C. J. & Dame, T. M. The Mass-Size Relation and the Constancy of GMC Surface Densities in the Milky Way. *Astrophys. J.* **898**, 3 (2020).
8. Williams, J. P., Blitz, L. & McKee, C. F. The Structure and Evolution of Molecular Clouds: from Clumps to Cores to the IMF. In Mannings, V., Boss, A. P. & Russell, S. S. (eds.) *Protostars and Planets IV*, 97 (2000).
9. Dobbs, C. L., Burkert, A. & Pringle, J. E. Why are most molecular clouds not gravitationally bound? *Mon. Not. R. Astron. Soc.* **413**, 2935–2942 (2011).
10. Pfalzner, S. *et al.* Observational constraints on star cluster formation theory. I. The mass-radius relation. *Astron. Astrophys.* **586**, A68 (2016).
11. Li, G.-X. Criteria for gravitational instability and quasi-isolated gravitational collapse in turbulent medium. *Mon. Not. R. Astron. Soc.* **465**, 667–671 (2017).
12. Cesarsky, C. J. & Volk, H. J. Cosmic Ray Penetration into Molecular Clouds. *Astron. Astrophys.* **70**, 367 (1978).
13. Crutcher, R. M. Magnetic Fields in Molecular Clouds. *Annu. Rev. Astron. Astrophys.* **50**, 29–63 (2012).
14. Kritsuk, A. G., Norman, M. L., Padoan, P. & Wagner, R. The Statistics of Supersonic Isothermal Turbulence. *Astrophys. J.* **665**, 416–431 (2007).
15. Li, G.-X. Scale-free gravitational collapse as the origin of $\rho \sim r^{-2}$ density profile - a possible role of turbulence in regulating gravitational collapse. *Mon. Not. R. Astron. Soc.* **477**, 4951–4956 (2018).
16. Donkov, S. & Stefanov, I. Z. Density distribution function of a self-gravitating isothermal compressible turbulent fluid in the context of molecular clouds ensembles. *Mon. Not. R. Astron. Soc.* **474**, 5588–5597 (2018).

17. Ungerechts, H. & Thaddeus, P. A CO Survey of the Dark Nebulae in Perseus, Taurus, and Auriga. *Astrophys. J. Suppl. Ser.* **63**, 645 (1987).
18. Dame, T. M., Hartmann, D. & Thaddeus, P. The Milky Way in Molecular Clouds: A New Complete CO Survey. *Astrophys. J.* **547**, 792–813 (2001).
19. Walter, F. M. & Boyd, W. T. Star Formation in Taurus-Auriga: The High-Mass Stars. *Astrophys. J.* **370**, 318 (1991).
20. Yang, Rui-zhi, de Oña Wilhelmi, Emma & Aharonian, Felix. Probing cosmic rays in nearby giant molecular clouds with the fermi large area telescope. *A&A* **566**, A142 (2014).
21. Planck Collaboration *et al.* Planck 2013 results. XI. All-sky model of thermal dust emission. *Astron. Astrophys.* **571**, A11 (2014).
22. Abdollahi, S. *et al.* Fermi large area telescope fourth source catalog. *The Astrophysical Journal Supplement Series* **247**, 33 (2020).
23. Liseau, R. *et al.* Gas and dust in the star-forming region ρ Oph A. The dust opacity exponent β and the gas-to-dust mass ratio g_{2d} . *Astron. Astrophys.* **578**, A131 (2015).
24. Huang, X., Yuan, Q. & Fan, Y.-Z. A GeV-TeV particle component and the barrier of cosmic-ray sea in the Central Molecular Zone. *Nature Communications* **12**, 6169 (2021).
25. Mercimek, S., Myers, P. C., Lee, K. I. & Sadavoy, S. I. An Estimation of the Star Formation Rate in the Perseus Complex. *Astron. J.* **153**, 214 (2017).
26. Arce, H. G. *et al.* Molecular Outflows in Low- and High-Mass Star-forming Regions. In Reipurth, B., Jewitt, D. & Keil, K. (eds.) *Protostars and Planets V*, 245 (2007).
27. Owen, E. R., On, A. Y. L., Lai, S.-P. & Wu, K. Observational Signatures of Cosmic-Ray Interactions in Molecular Clouds. *Astrophys. J.* **913**, 52 (2021).
28. Gabici, S., Aharonian, F. A. & Blasi, P. Gamma rays from molecular clouds. *Astrophys. Space Sci.* **309**, 365–371 (2007).
29. Veltchev, T. V., Donkov, S. & Klessen, R. S. Modelling the structure of molecular clouds - I. A multiscale energy equipartition. *Mon. Not. R. Astron. Soc.* **459**, 2432–2443 (2016).
30. Li, G.-X. & Burkert, A. Probing the multiscale interplay between gravity and turbulence - power-law-like gravitational energy spectra of the Orion Complex. *Mon. Not. R. Astron. Soc.* **464**, 4096–4106 (2017).
31. Li, G.-X. & Burkert, A. Quantifying the interplay between gravity and magnetic field in molecular clouds - a possible multiscale energy equipartition in NGC 6334. *Mon. Not. R. Astron. Soc.* **474**, 2167–2172 (2018).

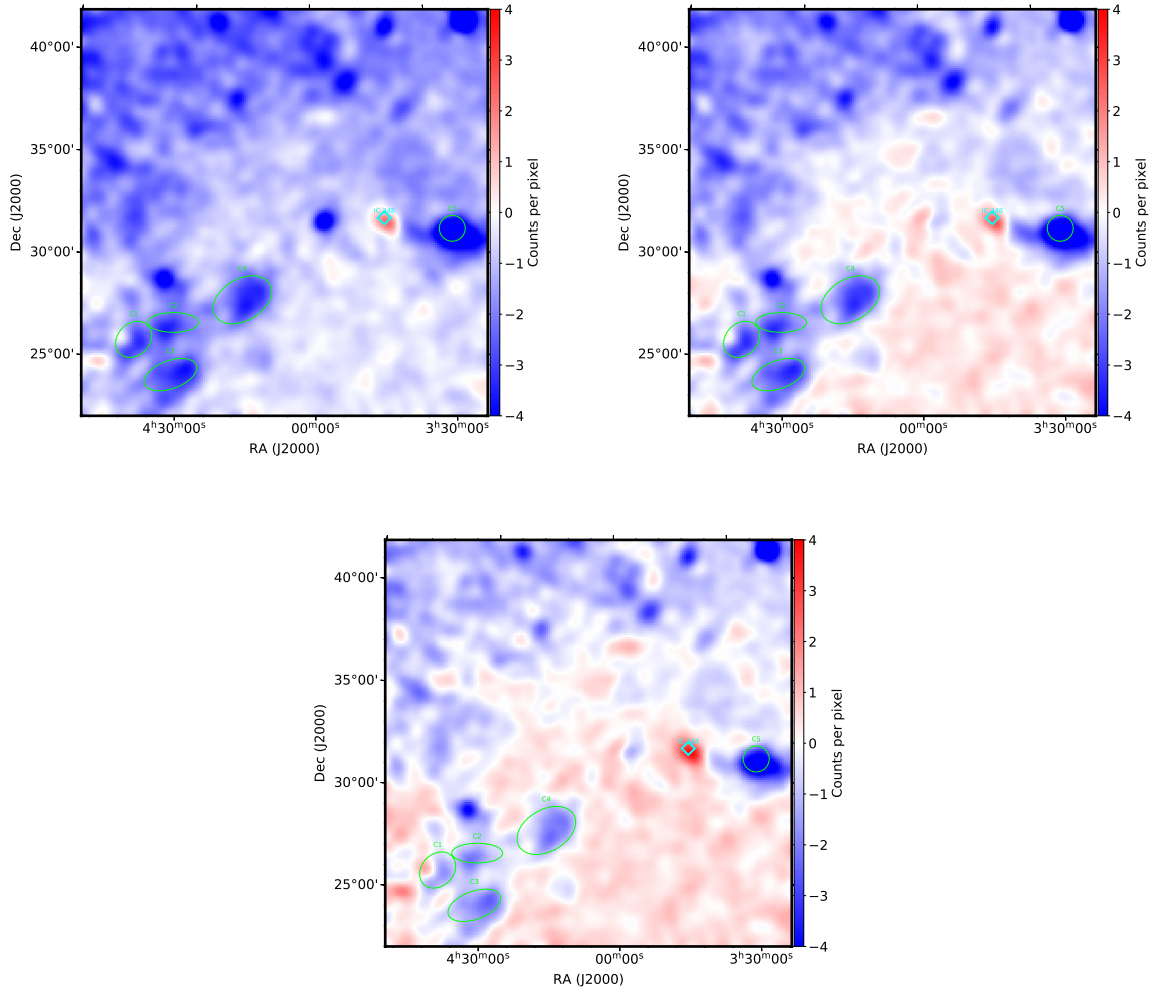
32. Berezhinskii, V. S., Bulanov, S. V., Dogiel, V. A. & Ptuskin, V. S. *Astrophysics of cosmic rays* (North-Holland, 1990).
33. Morlino, G. & Gabici, S. Cosmic ray penetration in diffuse clouds. *Mon. Not. R. Astron. Soc.* **451**, L100–L104 (2015).
34. Crutcher, R. M. Magnetic fields in molecular clouds. *Annual Review of Astronomy and Astrophysics* **50**, 29–63 (2012).
35. Dogiel, V. A. *et al.* Gamma-Ray Emission from Molecular Clouds Generated by Penetrating Cosmic Rays. *Astrophys. J.* **868**, 114 (2018).
36. Jiang, B. *et al.* Cavity of Molecular Gas Associated with Supernova Remnant 3C 397. *Astrophys. J.* **712**, 1147–1156 (2010).
37. Casse, F., Lemoine, M. & Pelletier, G. Transport of cosmic rays in chaotic magnetic fields. *Phys. Rev. D* **65**, 023002 (2001).
38. Fatuzzo, M., Melia, F., Todd, E. & Adams, F. C. HIGH-ENERGY COSMIC-RAY DIFFUSION IN MOLECULAR CLOUDS: A NUMERICAL APPROACH. *The Astrophysical Journal* **725**, 515–527 (2010).
39. Crutcher, R. M. Magnetic fields in molecular clouds: Observations confront theory. *The Astrophysical Journal* **520**, 706–713 (1999).
40. Urquhart, J. S. *et al.* ATLASGAL - towards a complete sample of massive star forming clumps. *Mon. Not. R. Astron. Soc.* **443**, 1555–1586 (2014).
41. Albertsson, T., Kauffmann, J. & Menten, K. M. Atlas of Cosmic-Ray-induced Astrochemistry. *Astrophys. J.* **868**, 40 (2018).
42. Ivlev, A. V. *et al.* Penetration of Cosmic Rays into Dense Molecular Clouds: Role of Diffuse Envelopes. *Astrophys. J.* **855**, 23 (2018).
43. Grenier, I. A., Casandjian, J.-M. & Terrier, R. Unveiling Extensive Clouds of Dark Gas in the Solar Neighborhood. *Science* **307**, 1292–1295 (2005).
44. Planck Collaboration *et al.* Planck early results. XIX. All-sky temperature and dust optical depth from Planck and IRAS. Constraints on the "dark gas" in our Galaxy. *Astron. Astrophys.* **536**, A19 (2011).
45. Vladimirov, A. E. *et al.* GALPROP WebRun: An internet-based service for calculating galactic cosmic ray propagation and associated photon emissions. *Computer Physics Communications* **182**, 1156–1161 (2011).
46. Ajello, M. *et al.* 3FHL: The Third Catalog of Hard Fermi-LAT Sources. *Astrophys. J. Suppl. Ser.* **232**, 18 (2017).

47. Lande, J. *et al.* Search for Spatially Extended Fermi Large Area Telescope Sources Using Two Years of Data. *Astrophys. J.* **756**, 5 (2012).
48. Abdo, A. A. *et al.* Fermi LAT Discovery of Extended Gamma-Ray Emission in the Direction of Supernova Remnant W51C. *Astrophys. J. Lett.* **706**, L1–L6 (2009).
49. Kafexhiu, E., Aharonian, F., Taylor, A. M. & Vila, G. S. Parametrization of gamma-ray production cross sections for p p interactions in a broad proton energy range from the kinematic threshold to PeV energies. *Phys. Rev. D* **90**, 123014 (2014).
50. Ackermann, M. *et al.* A Cocoon of Freshly Accelerated Cosmic Rays Detected by Fermi in the Cygnus Superbubble. *Science* **334**, 1103 (2011).
51. Yang, R.-z., de Oña Wilhelmi, E. & Aharonian, F. Diffuse γ -ray emission in the vicinity of young star cluster Westerlund 2. *Astron. Astrophys.* **611**, A77 (2018).
52. Yang, R.-z. & Aharonian, F. Diffuse γ -ray emission near the young massive cluster NGC 3603. *Astron. Astrophys.* **600**, A107 (2017).
53. Luhman, K. L., Esplin, T. L. & Loutrel, N. P. A Census of Young Stars and Brown Dwarfs in IC 348 and NGC 1333. *Astrophys. J.* **827**, 52 (2016).
54. Zucker, C. *et al.* A Large Catalog of Accurate Distances to Local Molecular Clouds: The Gaia DR2 Edition. *Astrophys. J.* **879**, 125 (2019).

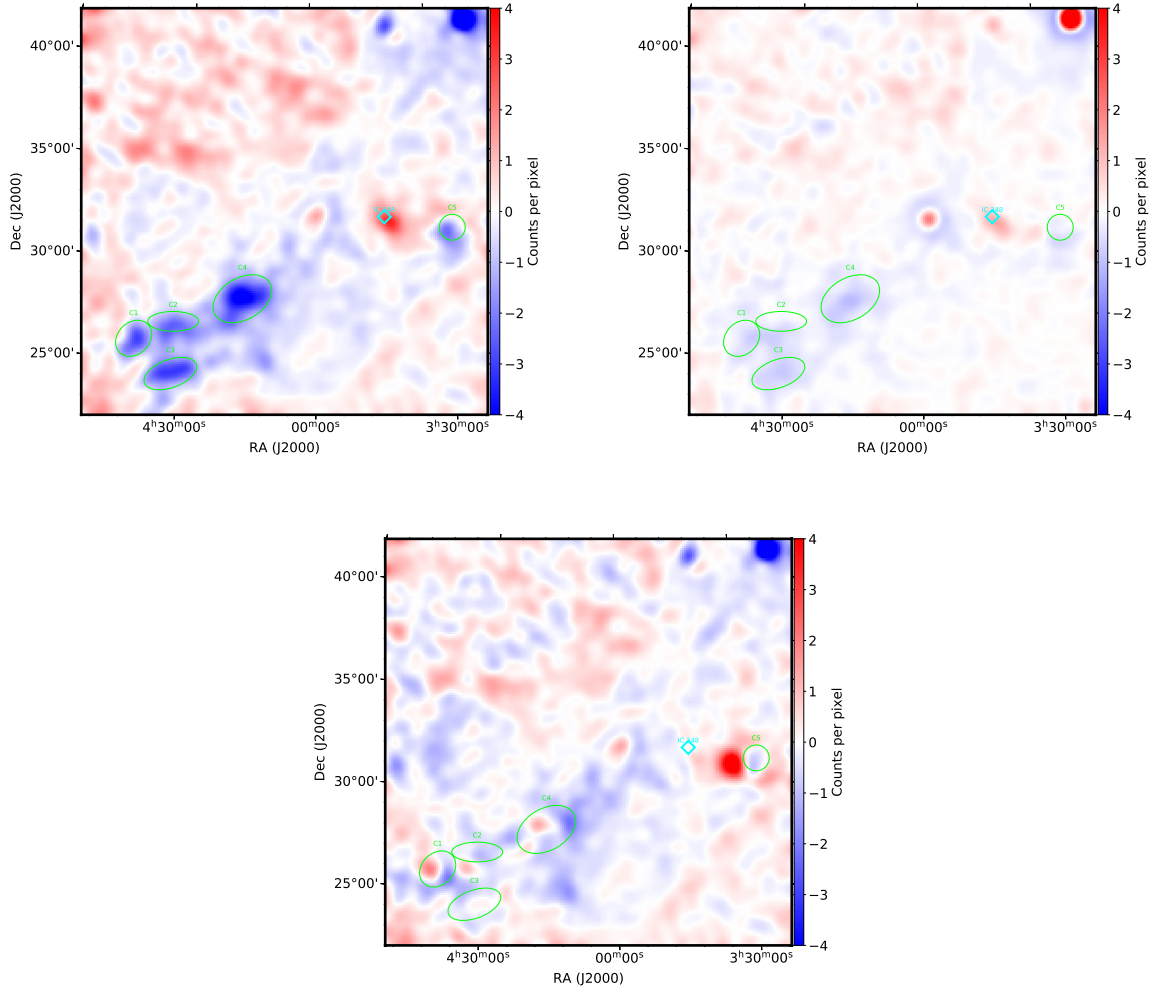
Model	event class	-log(likelihood)
dust	SOURCE	189284
dust + IC 348 disk	SOURCE	189259
dense + diffuse + IC 348 disk	SOURCE	188910
dust + IC 348 disk+6% bkg ¹	SOURCE	189271
dust + IC 348 disk-6% bkg ²	SOURCE	189271
dense + diffuse + IC 348 disk +6% bkg ¹	SOURCE	188917
dense + diffuse + IC 348 disk -6% bkg ²	SOURCE	188920
dust + IC 348 disk	PSF3	156161
dense + diffuse + IC 348 disk	PSF3	156095

1. 6% enhancement of diffuse background. 2. 6% decrease of diffuse background.

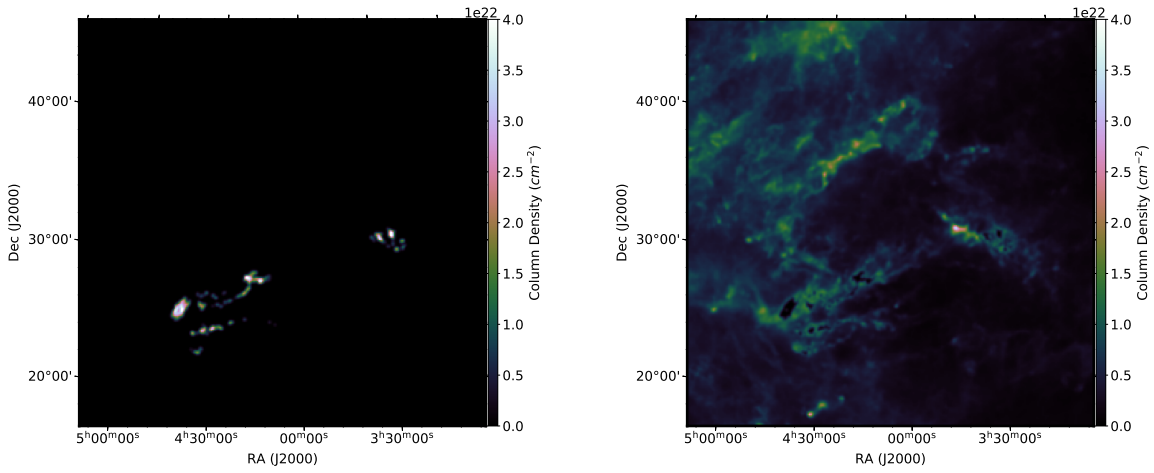
Supplementary Table 1: Fitting results for different models



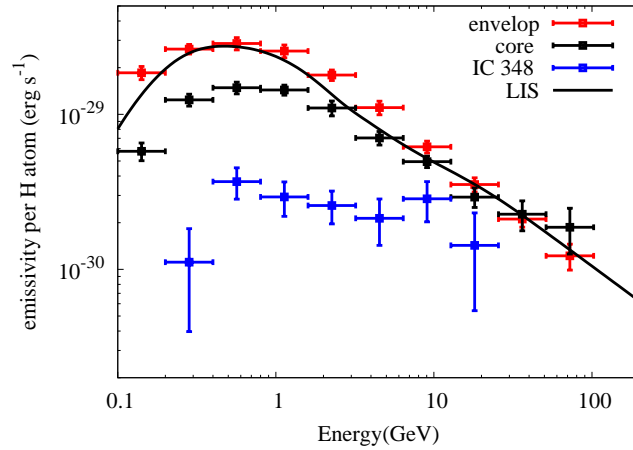
Supplementary Figure 1: The residual counts maps above 1 GeV in the $20^\circ \times 20^\circ$ region of Taurus and Perseus molecular clouds with pixel size corresponding to $0.1^\circ \times 0.1^\circ$, smoothed with a Gaussian filter of 0.3° . The top left panel shows the result for the best-fit Fermi background, while the top right and bottom panel show the results by artificially setting the normalization of the Galactic diffuse template to be 6% higher and lower than the best-fit value, respectively, during the fitting process. The cyan diamond label the position of IC 348. The green eclipses are the dense cores identified from dust opacity map.



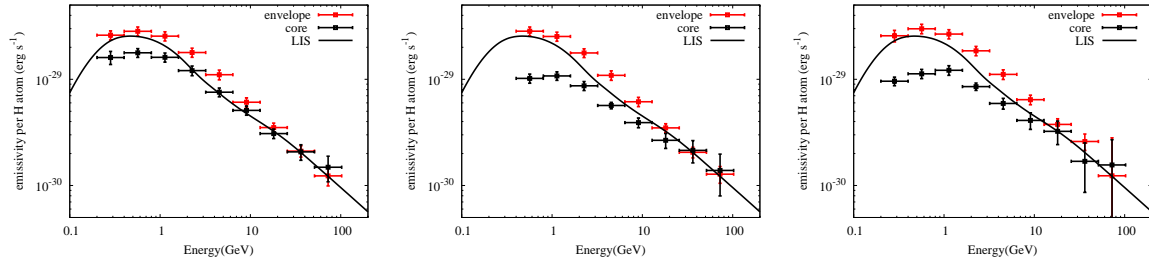
Supplementary Figure 2: The residual counts maps above 1 GeV in the $20^\circ \times 20^\circ$ region of Taurus and Perseus molecular clouds with pixel size corresponding to $0.1^\circ \times 0.1^\circ$, smoothed with a Gaussian filter of 0.3° . The top left panel shows the result of dust background with SOURCE event class, while the top right shows the result of dust background with PSF3 event class, and bottom panel shows the result for *dense+diffuse* model. The cyan diamond label the position of IC 348. The green eclipses are the dense cores identified from dust opacity map.



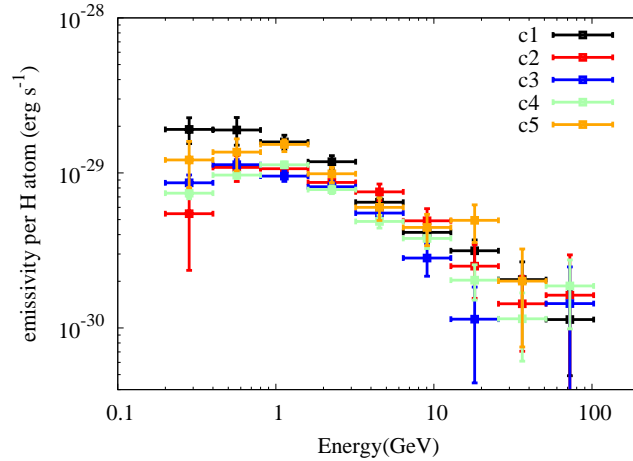
Supplementary Figure 3: The gas column density maps, which are used for gas templates in gamma-ray likelihood fittings, for dense core (left panel) and diffuse envelope (right panel).



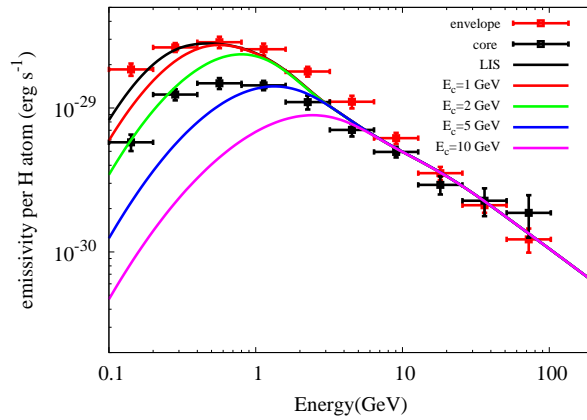
Supplementary Figure 4: The SEDs of gamma-ray emission of dense core (black), diffuse envelope (red) and the uniform disk surrounding HH211/IC 348 (blue). The x error bars represent the energy bin width, the y error bars are the $1 - \sigma$ statistical and systematic errors added in quadrature. The gamma-ray spectra have been normalized to gamma-ray emissivity per H atom. The black curve represents the predicted gamma-ray emissivity assuming the CR spectra is the same as the LIS.



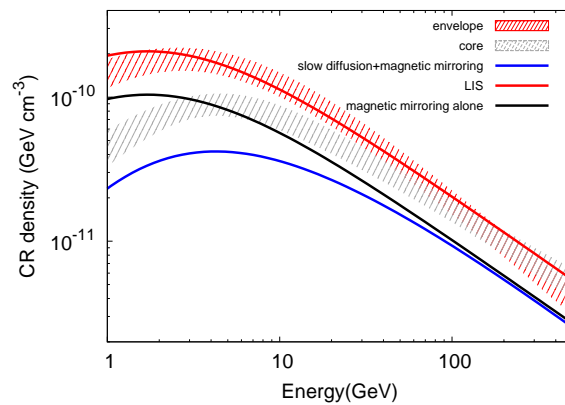
Supplementary Figure 5: The SEDs of gamma-ray emission of dense core (black), diffuse envelope (red). The x error bars represent the energy bin width, the y error bars are the $1 - \sigma$ statistical and systematic errors added in quadrature. The gamma-ray spectra have been normalized to gamma-ray emissivity per H atom. The black curve represent the predicted gamma-ray emissivity assuming the CR spectra is the same as the local interstellar spectra (LIS). The left panel shows the results assuming the *dense core* and *diffuse envelope* are separated at the the column density of $1.3 \times 10^{22} \text{ cm}^{-2}$, the middle panel shows the results assuming the *dense core* and *diffuse envelope* are separated at the the column density of $2.3 \times 10^{22} \text{ cm}^{-2}$, and the right panel show the results using the PSF3 datasets with *dense+diffuse* model of with the separation is done at $1.8 \times 10^{22} \text{ cm}^{-2}$.



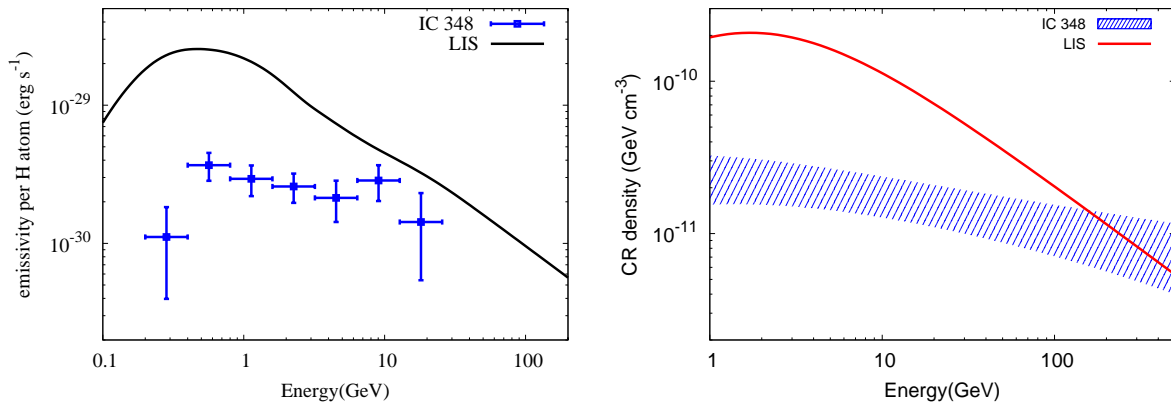
Supplementary Figure 6: The gamma-ray SEDs of individual clumps (C1-5). The x error bars represent the energy bin width, the y error bars are the $1 - \sigma$ statistical and systematic errors added in quadrature.



Supplementary Figure 7: The SED of gamma-ray emission of dense core (black), diffuse envelope (red). The gamma-ray spectra has been normalized to gamma-ray emissivity per H atom. The x error bars represent the energy bin width, the y error bars are the $1 - \sigma$ statistical and systematic errors added in quadrature. The curves are calculated assuming different sharp low energy cutoff of LIS.



Supplementary Figure 8: The derived CR spectra and the predicted CR spectrum taking into account magnetic focusing and mirroring. The two curves represent the case with and without the slow diffusion scenario. The shaded area represent the $1 - \sigma$ statistical and systematic errors for the derived CR density added in quadrature.



Supplementary Figure 9: left panel: The derived gamma-ray spectra normalized to gamma-ray emissivity per H atom for the IC 348 region. The x error bars represent the energy bin width, the y error bars are the $1 - \sigma$ statistical and systematic errors added in quadrature. The black curve represents the predicted gamma-ray emissivity assuming the CR spectra is the same as the LIS. right panel: derived CR energy density from the gamma-ray spectra. The black curve is the LIS. The shaded area represent the $1 - \sigma$ statistical and systematic errors for the derived CR density added in quadrature.